ANNUAL REVIEWS

Annual Review of Marine Science

Spaceborne Lidar in the Study of Marine Systems

Chris A. Hostetler,[1] Michael J. Behrenfeld,[2] Yongxiang Hu,[1] Johnathan W. Hair,[1] and Jennifer A. Schulien[2]

[1]Langley Research Center, National Aeronautics and Space Administration, Hampton, Virginia 23681-2199, USA; email: chris.a.hostetler@nasa.gov

[2]Department of Botany and Plant Pathology, Oregon State University, Corvallis, Oregon 97331-2902, USA

Annu. Rev. Mar. Sci. 2018. 10:121–47

First published as a Review in Advance on September 27, 2017

The *Annual Review of Marine Science* is online at marine.annualreviews.org

https://doi.org/10.1146/annurev-marine-121916-063335

Keywords

lidar, remote sensing, ocean plankton, atmospheric corrections, aerosols, clouds

Abstract

Satellite passive ocean color instruments have provided an unbroken ~20-year record of global ocean plankton properties, but this measurement approach has inherent limitations in terms of spatial-temporal sampling and ability to resolve vertical structure within the water column. These limitations can be addressed by coupling ocean color data with measurements from a spaceborne lidar. Airborne lidars have been used for decades to study ocean subsurface properties, but recent breakthroughs have now demonstrated that plankton properties can be measured with a satellite lidar. The satellite lidar era in oceanography has arrived. Here, we present a review of the lidar technique, its applications in marine systems, a perspective on what can be accomplished in the near future with an ocean- and atmosphere-optimized satellite lidar, and a vision for a multiplatform virtual constellation of observational assets that would enable a three-dimensional reconstruction of global ocean ecosystems.

1. INTRODUCTION

Fluorescence: absorption of a photon by an atom or molecule and subsequent emission of a photon as that atom or molecule relaxes back to a lower energy state

Marine ecosystems are complex entities that encompass vast numbers of species functioning over a wide range of spatial and temporal scales. Phytoplankton constitute the base of most marine ecosystems, and their annual net photosynthetic carbon fixation is roughly equivalent to that of all terrestrial plants (Field et al. 1998, Behrenfeld et al. 2001). This production at the base of the aquatic food chain drives CO_2 exchange between the atmosphere and ocean and fuels carbon sequestration in the deep sea (Falkowski et al. 1998, DeVries et al. 2012). Accordingly, plankton productivity plays a vital role in Earth's coupled ocean-atmosphere system. Furthermore, and in stark contrast to terrestrial vegetation, the entire global ocean phytoplankton stock is consumed and regrown every week (Antoine et al. 1996, Behrenfeld & Falkowski 1997). This rapid turnover underpins ocean food webs and, hence, fish stocks and global food supply. In addition, through an array of trophic interactions and metabolisms, some of the organic carbon products initially produced by phytoplankton are converted into volatilized molecules that leave the surface ocean and function as atmospheric aerosols that influence clouds and Earth's radiative budget (Meskhidze & Nenes 2006, Quinn & Bates 2011, Gantt & Meskhidze 2013, McCoy et al. 2015).

Satellite passive ocean color observations have vastly improved our understanding of global links between biodiversity, ecosystem structure, and ecological and biogeochemical function (McClain 2009). However, there are fundamental geophysical properties that simply cannot be characterized with ocean color technology alone (Section 2). Addressing these issues requires additional tools in space. For example, the Plankton, Aerosol, Cloud, and Marine Ecosystem (PACE) mission (NASA 2012) aims to co-deploy a multi-angle polarimeter with a hyperspectral ocean color sensor, with the polarimetry enabling more accurate atmospheric corrections and advanced characterization of ocean particle types (Loisel et al. 2008). Here, we describe how even greater synergies may be achieved by combining a passive ocean color sensor with an ocean-optimized satellite profiling lidar.

We begin this article with a brief review of the strengths and limitations of passive ocean color measurements (Section 2). We then present ocean lidar fundamentals (Section 3), describe airborne lidar measurements of ocean properties (Section 4), and summarize the current state of spaceborne lidar ocean remote sensing (Section 5). Our final sections describe an ocean-optimized, interdisciplinary lidar concept achievable in the near term (Sections 6 and 7) and introduce a multiplatform vision of synergistic space and field observations for global biogeochemical and ecosystem research (Section 8).

2. PASSIVE OCEAN COLOR: ADVANCES AND CHALLENGES

In the modern era of Earth system science, the availability of global satellite-based observations is all too easily taken for granted. But for the oceanographic community, such data are still a relatively new development, with the continuous global data record extending back less than 20 years. The Sea-Viewing Wide Field-of-View Sensor (SeaWiFS) was the first ocean color sensor to provide multiyear, fully global ocean color data. The SeaWiFS design was built on the proof-of-concept Coastal Zone Color Scanner (CZCS) and provided measurements at eight spectral bands, originally targeting a modest set of ocean geophysical properties (e.g., chlorophyll concentration). Subsequent missions [such as the Moderate Resolution Imaging Spectroradiometer (MODIS), the Medium Resolution Imaging Spectrometer (MERIS), and the Visible Infrared Imaging Radiometer Suite (VIIRS)] largely continued these heritage measurements, with some expansion (e.g., chlorophyll fluorescence bands on MODIS and MERIS) and improved spatial resolution and signal-to-noise ratio. The science community, by contrast, has greatly expanded the suite of retrieved ocean properties beyond the original targets.

Today, passive ocean color data are used to quantify surface-layer chlorophyll concentrations, particulate carbon stocks, and net primary production (McClain 2009). The development and application of spectral inversion algorithms to ocean color data have further provided assessments of absorption by colored dissolved organic matter (CDOM), phytoplankton absorption coefficients, total particulate backscatter coefficients (Garver & Siegel 1997; Lee et al. 2002; Maritorena et al. 2002; Siegel et al. 2002, 2005; Werdell et al. 2013), and estimates of phytoplankton carbon biomass and division rates (Behrenfeld et al. 2005, Westberry et al. 2008, Silsbe et al. 2016). The combination of fluorescence line height data and phytoplankton pigment and carbon data has yielded insights on iron stress and photophysiology (Behrenfeld et al. 2009, Westberry et al. 2013, Lin et al. 2016). Additional algorithm development has led to new retrievals regarding plankton community composition, including phytoplankton size fractions, the slope of the particle size distribution, and even specific phytoplankton groups, such as coccolithophores, *Trichodesmium*, and harmful algal species (e.g., Alvain et al. 2005, Bracher et al. 2009, Kostadinov et al. 2010, Sadeghi et al. 2012, Sathyendranath et al. 2014 and references therein). Furthermore, the sustained time series of these diverse ocean properties has provided major advances in our understanding of plankton annual cycles and responses to climate variations and has been instrumental for informing and testing ocean ecosystem models. Quite simply, the satellite ocean color record has fostered a major revolution in oceanography.

Optical depth: the product of physical depth and attenuation coefficient; over 1 optical depth, a radiant flux is reduced by 63%

Despite the advances enabled through ocean color observations, the passive radiometric technique has several fundamental limitations. Specifically, (*a*) the top-of-atmosphere signal measured by the sensors includes contributions from sources other than the target ocean properties, (*b*) the ocean color signal provides no information on the vertical distribution of ocean constituents, (*c*) measured ocean color is an optically integrated property without a direct signal for separating the absorption and scattering fractions, and (*d*) global sampling is compromised by atmospheric interferences and solar angle. The following provides additional detail on these limitations.

Large uncertainties in passively retrieved ocean parameters can result from atmospheric correction errors. Radiances measured by ocean color instruments include, beyond the targeted ocean properties, contributions from subsurface bubbles, surface foam, reflection from the ocean surface, and atmospheric constituents, including aerosols, clouds, and air molecules. Easily 90% of the top-of-atmosphere measured signal can be due to scattering from the atmosphere. A small error in the estimation and removal of this atmospheric contribution creates a large relative error in the estimated water-leaving radiances and associated geophysical retrievals. Similarly, unaccounted-for contributions from bubbles, foam, and surface reflection degrade retrieval fidelity. Under particularly challenging conditions (e.g., sunglint, significant aerosol loads, or nearby clouds), attempts to retrieve ocean properties are abandoned all together.

The ocean color signal is also heavily weighted toward the surface. This results from the exponential decay of sunlight with depth caused by absorption from water, particles, and dissolved matter. Similarly, the up-scattered photons suffer the same exponential decay on their path to the ocean surface. The result is that more than 92% of the ocean color signal emanates from the first optical depth (10-m geometric depth if the diffuse attenuation coefficient $= 0.1\ m^{-1}$), and 71% comes from the first half of the first optical depth (5 m for the same case). This limitation of ocean color can result in significant errors in important water column–integrated ocean properties, such as chlorophyll concentration (Sathyendranath & Platt 1989, Stramska & Stramski 2005) or net primary production (Platt & Sathyendranath 1988, Churnside 2015, Jacox et al. 2015).

A further challenge with passive ocean color data is that the strength and spectral characteristics of retrieved water-leaving radiances represent the integrated signature of multiple factors. Dominant contributors to the signal include backscattering by suspended particles (b_{bp}) and absorption by colored dissolved matter (a_{cdm}), phytoplankton pigments (a_{ph}), and nonalgal particles

(a_{nap}) (note that the absorption and scattering by salt water is a known function of salinity). Retrievals of these four fundamental properties and other geophysical parameters derived from them have an inherent uncertainty that cannot be reduced without additional information. This issue is a driving motivation for the PACE mission's expanded measurement spectral range and resolution compared with heritage ocean color missions. Coupling such passive ocean color measurements with active satellite instruments can likewise reduce uncertainties in derived ocean properties.

Finally, satellite ocean color sampling is significantly limited by atmospheric interferences and sun angle. On average, clouds obscure 70% of Earth's ocean area from passive ocean retrievals. Broken cloud scenes are a significant fraction of the remaining ocean area, and under these conditions, side scatter from nearby clouds can compromise accurate ocean retrievals from otherwise clear sky pixels. Beyond issues of cloudiness, ocean color retrievals must be abandoned when strongly scattering aerosol layers are present. Some of these aerosol interferences can compromise ocean color monitoring for extended periods. Examples of such conditions include pollution outflow from populated regions (e.g., the US Eastern Seaboard, India, and China), systematic dust events (e.g., Saharan dust outflow at low northern latitudes in the Atlantic and Gobi dust outflow at midlatitudes in the North Pacific), and long-range and broadly distributed smoke transport (e.g., from boreal forest fires in North America and Siberia and agricultural fires from all continents). In polar regions, low sun angles and cloud conditions (i.e., cloud shadowing of otherwise clear pixels) can eliminate ocean color sampling altogether from late fall through early spring. Notably, these high-latitude regions include some of the most productive waters in the global oceans, and the lack of sampling for a significant fraction of the year can undermine any complete understanding of plankton annual cycles and biogeochemistry (Behrenfeld et al. 2017).

The intent of this section is not to criticize the passive ocean color approach, but rather to recognize both its benefits and its inherent weaknesses and thereby highlight where additional technologies may contribute to improve understanding of global ocean ecosystems. Passive ocean color radiometry has enabled huge scientific advances and will remain a cornerstone of future global ocean research. With increases in spectral coverage and resolution from missions like PACE and work toward increasing the number and coverage of geostationary sensors like the Geostationary Ocean Color Imager (GOCI) (Ryu et al. 2012, O'Malley et al. 2014), the ocean color portfolio is set to expand significantly. It is time to consider complementary remote sensing techniques that will enable additional breakthrough science on issues beyond the reach of passive radiometry. Lidar is just such a technique and can usher in the next revolution in satellite ocean remote sensing.

3. LIDAR 101

Airborne lidars have been used for decades to study the atmosphere and the oceans. However, a long-standing question has been whether space-borne lidars can achieve the sensitivity required to provide useful ocean products. That question was answered decisively with data from the Cloud Aerosol Lidar with Orthogonal Polarization (CALIOP) instrument, which has operated in space since 2006 on the Cloud Aerosol Lidar and Infrared Pathfinder Satellite Observation (CALIPSO) platform (Winker et al. 2009). CALIOP is one of the instruments in the A-Train satellite constellation (which includes MODIS) and was designed solely for atmospheric measurements, not as an ocean lidar. Nevertheless, Hu (2009) developed an innovative technique for retrieving ocean subsurface particulate backscatter from CALIOP data. But before telling the story of ocean science breakthroughs made with CALIOP, we provide here some background explanation of the lidar technique.

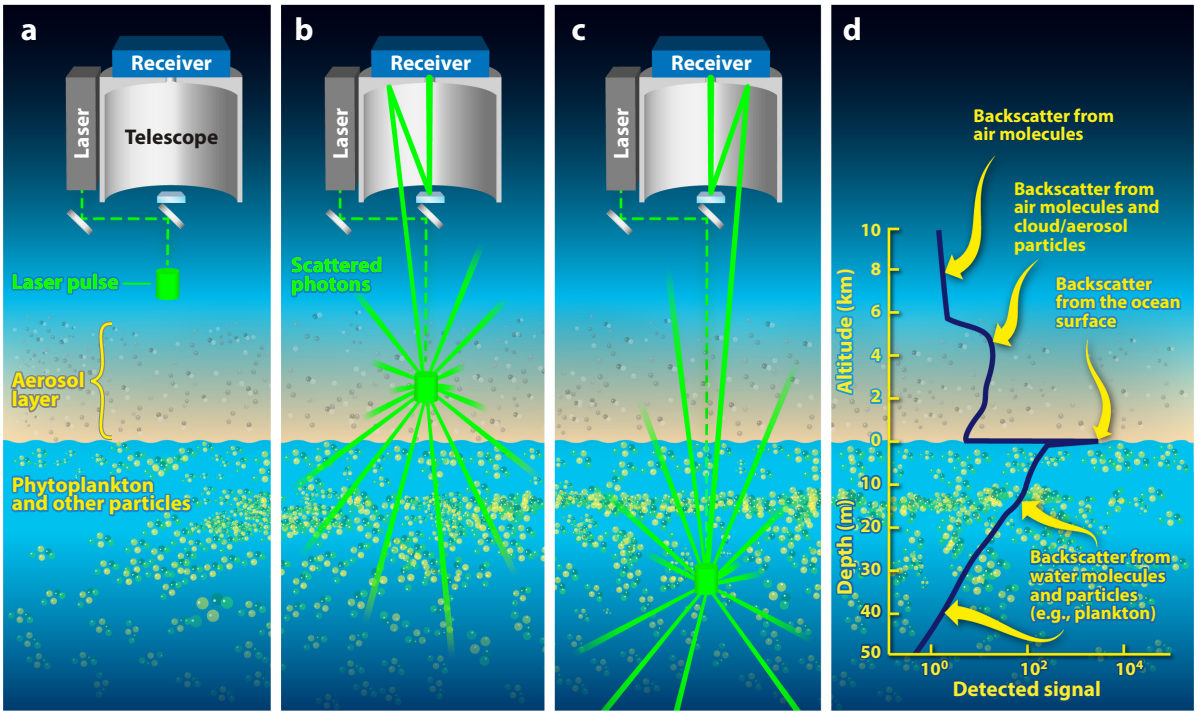

Figure 1

Illustration of the lidar time-of-flight ranging technique. (*a*) The laser transmits a short (e.g., 15 ns) pulse of laser light that is directed downward. (*b*) As the laser pulse travels toward Earth, photons are scattered from air molecules and cloud/aerosol particles in the atmosphere. (*c*) Shortly thereafter, the pulse penetrates the ocean, where photons are scattered by water molecules and suspended particles. Some of the scattered photons in the atmosphere and ocean are collected by the telescope, and the magnitude of this signal is recorded as a function of time by detectors located in the receiver. (*d*) Using the speed of light, time is converted to distance, creating a vertically resolved profile of received backscatter.

Lidar is an acronym for light detection and ranging. Similar to radar, it employs a time-of-flight technique to provide range-resolved (i.e., for the current discussion, vertically resolved) measurements of optical properties. Unlike the ocean color technique's reliance on the sun as a source of light (thus the term passive remote sensing), lidar uses lasers to generate its own photons, which are ultimately scattered back to the instrument's receiver (thus the term active remote sensing). Because of their durability, the most common lasers used in field-deployed and spaceborne lidar systems are Nd:YAG lasers, which have a fundamental emission at 1,064 nm and can be frequency doubled and tripled to 532 and 355 nm, respectively. **Figure 1** provides a simple illustration of the lidar approach, where the geometry depicted is a nadir-viewing configuration. In this example, laser pulses are directed downward, and a small fraction of the backscattered light is collected in a telescope receiver. In the atmosphere, this backscattered light originates from air molecules and suspended particles, such as cloud droplets or aerosol particles. Similarly, photons from the laser pulse are backscattered in the ocean by water molecules and suspended particles, such as phytoplankton. These signals are received by the telescope and imaged onto a high-speed optical detector.

Nd:YAG laser: a solid-state laser employing neodymium-doped yttrium aluminum garnet as the gain medium

This lidar detector generates a time-varying electrical signal that is proportional to the instantaneous optical power incident on the detector, and this electrical signal is recorded at a high sampling rate (e.g., 10^7–10^8 samples per second). The point of origin of the signal (in other words, its vertical position in the atmosphere or ocean) is determined using the speed of light. Specifically,

each sample is assigned a distance from the lidar based on the time difference between the firing of the laser and the detection of the backscattered signal. Sequential recording of all of these samples into a data array creates a vertically resolved profile, with each sample reflecting the magnitude of scattering at a known altitude in the atmosphere or depth into the ocean (**Figure 1*d***). Importantly, the vertical resolution of a lidar profile is determined by the rate of sampling by its detector. For example, a rate of 10^7 samples per second corresponds to the 15-m vertical resolution commonly used for atmospheric measurements, whereas a rate of 10^8 samples per second would correspond to an ∼1-m vertical resolution that is more appropriate for ocean profiling.

From each laser pulse, a lidar acquires a single vertical profile of the atmosphere and ocean. Combining data from multiple laser pulses creates a time series of profiles. When a lidar is mounted on a moving platform, such as an aircraft or satellite, this time series maps to a horizontally and vertically resolved data curtain registered to the flight track (an example is shown in Section 4). One advantage of active lidar remote sensing is that it creates these curtains of data both day and night, thus providing opportunities to study diel changes in plankton properties and to continue observations during periods of polar night. During daylight hours, the contribution to the received signal from diffusely scattered sunlight is estimated from data acquired between laser pulses and subtracted from the measured profiles.

Producing useful geophysical data products from the measured lidar signals requires application of appropriate calibration factors and postprocessing algorithms. Perhaps more importantly, the suite of products that can be produced and their accuracy depend on instrument design (e.g., the number and character of the receiver channels). Our illustration (**Figure 1**) and discussion to this point has centered on what is termed the elastic backscatter lidar technique. This technique relies on backscatter from air and seawater molecules and particles at the same wavelength as the transmitted laser pulse. In its simplest configuration, an elastic backscatter lidar measures attenuated backscatter, from which particulate backscatter and attenuation coefficients are estimated (see the sidebar titled What Does Backscatter Lidar Measure?).

Field-deployed ocean lidars typically expand measurement capabilities beyond those of the system illustrated in **Figure 1** by including additional design elements. Important examples include the addition of receiver channels that measure laser-induced fluorescence and wavelength-shifted Raman scattering from specific ocean constituents. Another example is the addition of channels to measure the polarization of backscattered photons. Lidars capable of generating an array of geophysical data products have been demonstrated for decades from stationary platforms, ships, and aircraft. Scientific progress made with airborne lidars motivates some of our thinking about a future ocean-optimized satellite lidar and is discussed in the next section.

4. ESSAYS FROM THE FIELD

Although elastic backscatter lidar is the simplest technique, the first scientifically meaningful oceanographic applications of airborne lidar involved the use of fluorescence techniques, first with chlorophyll (Kim et al. 1973) and later with CDOM (Hoge et al. 1995). The strength of the chlorophyll fluorescence signal is determined by the concentration of chlorophyll in the water and by physiological variations in the quantum yield of fluorescence (Behrenfeld et al. 2009). Chlorophyll readily absorbs light at 532 nm, which is a commonly transmitted wavelength for Nd:YAG-based ocean lidars. A fraction of this absorbed light energy is re-emitted as fluorescence in the 670–690-nm region. Detecting this signal alone does not provide a useful measurement, however. One must correct the magnitude of signal for factors that are unrelated to phytoplankton, such as variations in laser energy, atmospheric attenuation, and water attenuation. These corrections can be made by dividing the measured fluorescence by Raman-shifted backscatter

WHAT DOES BACKSCATTER LIDAR MEASURE?

An elastic backscatter lidar (**Figure 1**) measures a signal (S) that is proportional to attenuated backscatter, which is the sum of the 180° backscatter from water molecules (β_M) and suspended particles (β_P) multiplied by the two-way transmittance of the intervening atmosphere and ocean between the lidar and the water volume at a particular depth, z. The vertical profile of this retrieved signal, $S(z)$, is defined by

$$S(z) = \begin{pmatrix}\text{lidar}\\ \text{instrument}\\ \text{constant}\end{pmatrix}\begin{pmatrix}\text{telescope}\\ \text{perception}\\ \text{angle}\end{pmatrix}\begin{pmatrix}\text{molecular plus}\\ \text{particulate}\\ \text{backscatter}\end{pmatrix}\begin{pmatrix}\text{one-way}\\ \text{seawater}\\ \text{transmittance}\end{pmatrix}^2\begin{pmatrix}\text{one-way}\\ \text{atmospheric}\\ \text{transmittance}\end{pmatrix}^2,$$

$$S(z) = C_L\left[\frac{A}{(nH+z)^2}\right][\beta_M(z)+\beta_P(z)]\left\{\exp\left[-\int_0^z K_L(z')dz'\right]\right\}^2(T_A)^2,$$

where C_L is the lidar instrument constant (a function of instrument parameters such as laser energy, the optical efficiency of the receiver, and detector electronic gain), A is the telescope area, H is the height of the lidar above the ocean, n is the index of refraction of water, K_L is the attenuation coefficient of the lidar signal, and T_A is the transmission of the atmosphere. This equation is then used to solve for the two unknowns of interest, β_P and K_L.

Common oceanographic properties relevant to the lidar measurement are the hemispheric particulate backscatter coefficient, b_{bp}, and the downwelling irradiance attenuation coefficient, K_D. Throughout this review, we discuss lidar retrievals of b_{bp}. Values of b_{bp} are derived from lidar β_P at 180° by applying a scattering phase function (e.g., Boss & Pegau 2001) in the same manner that b_{bp} is calculated from single-angle measurements of backscatter from in situ instruments. As discussed in detail by Gordon (1982), the relationship between K_D and K_L is dependent on the optical properties of the water and the viewing geometry of the lidar. Specifically, K_L approaches K_D as either the attenuation coefficient increases or the diameter of the ocean surface viewed by the lidar increases. For airborne lidar measurements with narrow fields of view, K_L will exceed K_D under clear open ocean conditions. For satellite observations, the diameter of the lidar viewing area is sufficiently large that retrieved K_L is an excellent proxy for K_D. Accordingly, we use the notation K_L in this review when referring to airborne retrievals of attenuation and K_D for satellite retrievals.

from water molecules measured at a different wavelength (Bristow et al. 1981) under the assumption that the above-mentioned factors unrelated to chlorophyll cancel in the ratio (Poole & Esaias 1982). The Raman signal results from the laser exciting the O-H vibrational stretching mode of water molecules, which causes a frequency shift of 3,418 cm^{-1} for a fraction of the scattered photons (for 532-nm laser excitation, the Raman-shifted water backscatter is at 645 nm). The Raman correction yields a relative, rather than absolute, measure of chlorophyll fluorescence.

Some of the most significant lidar-based field studies of chlorophyll fluorescence were made by a research group at the NASA Wallops Flight Facility using their Airborne Oceanographic Lidar (AOL) (Hoge & Swift 1981). That lidar employed a grating spectrometer in the receiver to isolate the chlorophyll fluorescence and Raman-shifted water backscatter. This water-Raman-normalized chlorophyll fluorescence signal was used in many studies. For instance, Yoder et al. (1993) used chlorophyll fluorescence signals acquired with the AOL during flights on a long-range P-3B aircraft to study spatial scales of the North Atlantic bloom. From these measurements, they concluded that the pixel resolution of a typical global ocean color satellite mission captures the dominant scales of variability in the bloom and that mesoscale variability must be taken into account in the interpretation of ship-based measurements to avoid confusing changes caused by advection

with those caused by local ecosystem processes. Martin et al. (1994) used data from AOL during the Iron Enrichment Experiment (IronEx) to test the hypothesis that iron is a limiting factor for phytoplankton productivity in the equatorial Pacific. AOL fluorescence data were further used by Hoge et al. (2003) to validate MODIS ocean color fluorescence line height products. Hoge et al. (2005) subsequently used both AOL chlorophyll and CDOM fluorescence measurements to quantify chlorophyll biomass, using a modification of an ocean color algorithm and matchup data with ship-based in situ measurements to appropriately scale their fluorescence-to-Raman ratios. Because fluorescence lidar signals are weak and decay rapidly with depth, the total vertically integrated fluorescence signals were used in these studies rather than the noisier depth-resolved profiles.

True water column profiling measurements were first made possible with the elastic backscatter lidar technique described in Section 3. An excellent review article by Churnside (2014) provides a detailed technical description of the elastic backscatter technique and an overview of the modeling and interpretation of backscatter signals. Airborne implementations of this technique were demonstrated in the late twentieth century by groups from around the world, including Australia (Billard et al. 1986), the United States (Hoge et al. 1988), Russia (Bunkin & Surovegin 1992), and Sweden (Steinvall et al. 1993). A major challenge to this technique is ambiguity in the interpretation of the measured signal. The magnitude of the measured signal depends on several known parameters (e.g., range and molecular density) and several unknowns: the lidar instrument constant, the atmospheric transmittance, and the ocean parameters of interest, β_P and K_L (see the sidebar titled What Does Backscatter Lidar Measure?). With one measured property (relative attenuated backscatter) and several unknowns, the elastic backscatter lidar retrieval is an ill-posed problem.

Additional information content was achieved with the addition of polarization sensitivity. This involves transmitting a linearly polarized laser pulse and optically separating the received backscatter into components polarized parallel (a co-polarized channel) and perpendicular (a cross-polarized channel) to that of the pulse (Churnside 2008, 2014). The polarization of 180° backscatter from water molecules and spherical particles is parallel to that of the transmitted laser pulse and is received in the co-polarized channel. Nonspherical particles, like many phytoplankton, partially randomize the polarization of scattered photons such that most of the backscatter is received in the co-polarized channel, and a smaller but measurable signal is received in the cross-polarized channel. Received photons arising from two or more scattering events are also somewhat randomized in polarization, regardless of particle shape. Thus, unlike the co-polarized channel, for which there is ambiguity in the relative contributions of molecular and particulate scattering, the cross-polarized channel is a more direct measurement of attenuated particulate backscatter. However, the degree to which the laser pulse is depolarized depends, for example, on the size and shape of the particles and the relative contributions from multiple scattering events. Challenges also remain with instrument calibration for both channels and accurate separation of depth-dependent changes in backscatter from those in attenuation. Because of these issues, early results were typically confined to relative, rather than absolute, backscatter and depth-averaged estimates of K_L.

Scientific application of elastic backscatter lidar began to flourish only in the last decade, largely based on the work of James Churnside and extensive deployments of the National Oceanic and Atmospheric Administration (NOAA) Fish Lidar (Churnside et al. 2001). This lidar was originally designed for the detection and quantification of fish schools (Churnside et al. 1997, 2001, 2003) but was later applied to retrieving ocean inherent optical properties. Early scientific contributions that used the NOAA lidar included several studies of subsurface plankton layers (e.g., Churnside & Ostrovsky 2005, Churnside & Donaghay 2009). More recently, the focus has been on overcoming the ambiguity in the elastic backscatter retrieval through bio-optical modeling. Churnside et al. (2014) employed a parameterization based on chlorophyll concentration to estimate the ratio of attenuation to backscatter, thereby reducing the retrieval of β_P and K_L to solving for a

HIGH-SPECTRAL-RESOLUTION LIDAR: TWO MEASUREMENTS, TWO UNKNOWNS

HSRL designs vary from instrument to instrument, but the fundamental approach is the same. We consider here the simplest of HSRL architectures, which has two detection channels. One of these channels is more sensitive to particulate backscatter from the ocean (the middle peak in **Figure 2**), and one is more sensitive to molecular backscatter from seawater itself (the right and left peaks in **Figure 2**). This separation of the backscatter signal is accomplished in the lidar receiver (**Figure 1**) with a spectral filter (e.g., an interferometer) that has a well-characterized frequency response. The two time-resolved signals are algebraically combined to form two profiles proportional to backscatter at 180°. The first of these derived profiles, $S_M(z)$, represents photons backscattered by water (β_M):

$$S_M(z) = C_M \left[\frac{A}{(nH + z)^2}\right] \beta_M \left\{ \exp\left[-\int_0^z K_L(z')dz'\right]\right\}^2 (T_A)^2,$$

where C_M incorporates instrument constants relevant to this molecular profile reconstruction. The second profile, $S_P(z)$, represents photons backscattered by suspended particles in the ocean (β_P):

$$S_P(z) = C_P \left[\frac{A}{(nH + z)^2}\right] \beta_P(z) \left\{ \exp\left[-\int_0^z K_L(z')dz'\right]\right\}^2 (T_A)^2,$$

where C_P is the instrument constant for the particulate profile reconstruction. Because the density of seawater molecules is relatively constant in the near-surface ocean, the value of β_M is well known. Thus, the value of K_L can be calculated from changes in $S_M(z)$ from one depth interval to the next through the water column:

$$K_L(z) = -\frac{1}{2}\frac{d}{dz}\ln\left[(nH + z)^2\, S_M(z)\right].$$

Importantly, the influence of attenuation, K_L, and atmospheric transmission, T_A, are the same for $S_P(z)$ and $S_M(z)$. Consequently, these two terms cancel in the ratio $S_P(z)$:$S_M(z)$, allowing the attenuation-corrected profile of particulate backscatter at 180° to be calculated as

$$\beta_P(z) = \beta_M \left[\frac{C_M}{C_P}\right]\left[\frac{S_P(z)}{S_M(z)}\right],$$

where the only scaling factors required are estimates of β_M (well known) and the C_M:C_P ratio (which can be determined with high accuracy). β_P is then scaled to hemispheric backscatter, b_{bp} (see the sidebar titled What Does Backscatter Lidar Measure?).

In summary, the power of the HSRL technique is that it provides two measurements to solve for two unknowns and requires only relative (i.e., the C_M:C_P ratio), rather than absolute, calibration. This contrasts critically with the elastic backscatter lidar technique, which provides only the combined $S_P(z) + S_M(z)$ profile and therefore requires absolute calibration, correction for the atmospheric transmission, and either ancillary data or model assumptions about the relationship between b_{bp} and K_L to retrieve either one.

single unknown, as is done for vertically resolved atmospheric aerosol retrievals (Fernald 1984). Churnside (2015) extended this bio-optical approach with an iterative scheme that also enabled the retrieval of chlorophyll concentration. This technique was then used to study plankton layers in the Arctic (Churnside & Marchbanks 2015) and vertical distributions of primary production (Churnside 2016).

Application of bio-optical modeling advanced the elastic backscatter lidar technique from retrievals of relative backscatter and depth-averaged attenuation to quantitative depth-resolved ocean properties. However, the impact of errors in the chlorophyll-based parameterization has not

been assessed. The two parameterized unknowns, β_P and K_L, can vary independently (e.g., with CDOM concentration) (Siegel et al. 2005). This affects K_L but not β_P and violates the retrieval assumptions. Unfortunately, retrieval errors also accumulate as the retrieval proceeds downward through the profile, because the error at a particular depth interval is a function not only of the retrieval error for that interval, but also of the accumulated error from intervals higher in the column. Furthermore, the fundamental problem of absolute calibration of the ocean signal remains. Calibration in this sense includes quantifying the product of the square of the atmospheric transmittance and the instrument constant (see the sidebar titled What Does Backscatter Lidar Measure?). For the typical 300-m flight altitude of many airborne ocean lidars, the near-unity atmospheric transmittance can be estimated with little error, and the instrument constant can be determined using preflight measurements (Lee et al. 2013). However, a satellite lidar retrieval of ocean properties must account for the transmittance of the entire atmosphere, which changes continuously along the orbit track owing to highly variable aerosol and cloud layers. Consequently, the simple calibration approach used for low-altitude aircraft measurements cannot be applied in space without large errors in retrieved ocean properties.

A significant leap in retrieval accuracy and information content has recently been made by applying the high-spectral-resolution lidar (HSRL) technique to ocean profiling. This technique has been used for decades in ground-based (e.g., Shipley et al. 1983) and airborne (Esselborn et al. 2008, Hair et al. 2008, Bruneau et al. 2015) aerosol and cloud measurements. It is based on the difference in the wavelength distributions of backscatter from particles and molecules (**Figure 2**). Backscatter from particles occurs at the same wavelength as the transmitted laser pulse. By contrast, backscatter from molecules, such as seawater, is shifted and broadened in wavelength owing to interactions between the transmitted pulse and density fluctuations from sound waves (Hickman et al. 1991). This phenomenon is known as Brillouin scattering, and at 532 nm, the wavelength

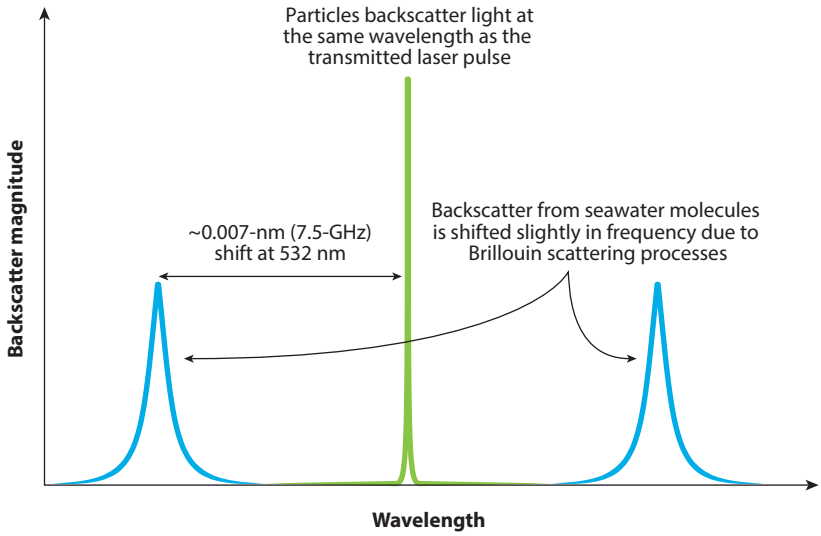

Figure 2

The high-spectral-resolution lidar technique (see the sidebar titled High-Spectral-Resolution Lidar: Two Measurements, Two Unknowns). This method relies on the spectral separation between 180° backscatter from seawater and suspended particles (e.g., phytoplankton). The spectrum of particulate backscatter (*green*) is nearly identical to that of the transmitted single-frequency laser pulse. Molecular backscatter (*blue*), by contrast, is shifted (by ~0.007 nm or 7.5 GHz at 532 nm) and broadened by Brillouin scattering processes.

shift is approximately 0.007 nm (**Figure 2**). This separation of water and particulate backscatter is fundamental to the HSRL technique. It provides two lidar profiles from which to retrieve the two unknowns, β_P and K_L, thus enabling a well-posed rather than ill-posed retrieval, as discussed in the sidebar titled High-Spectral-Resolution Lidar: Two Measurements, Two Unknowns. Also discussed in the sidebar is the equally important calibration accuracy of the HSRL technique. The particulate backscatter retrieval depends on instrument constants only and is not affected by variability in atmospheric transmittance.

The first HSRL retrievals of diffuse attenuation, K_L, and particulate backscatter, b_{bp}, were made during the 2012 Azores campaign (Behrenfeld et al. 2013), the 2014 Ship-Aircraft Bio-Optical Research (SABOR) experiment (Hair et al. 2016, Schulien et al. 2017), and the 2015 and 2016 North Atlantic Aerosols and Marine Ecosystems Study (NAAMES) deployments. **Figure 3** shows atmospheric and ocean retrieval curtains from a flight of the NASA HSRL-1 instrument during

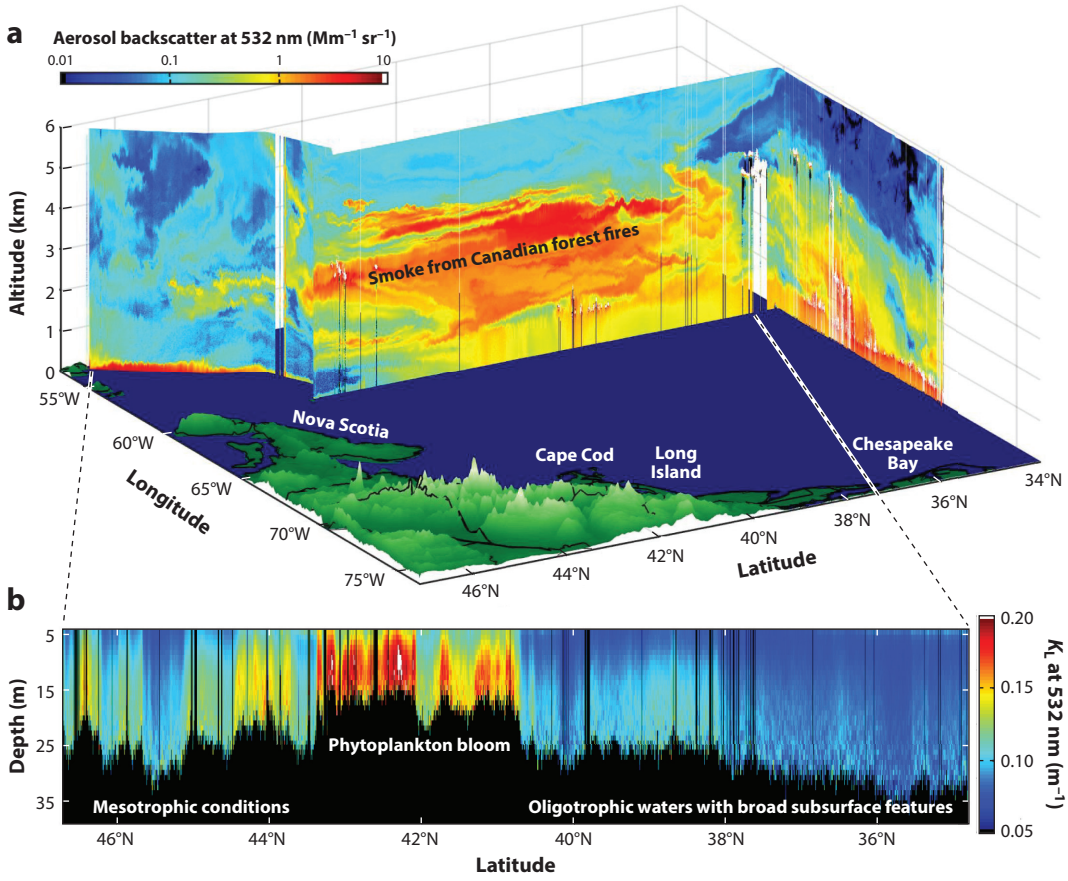

Figure 3

Along-track curtain plots acquired with the NASA airborne HSRL-1 instrument in May 2016 during a NAAMES deployment. (*a*) Vertically resolved aerosol backscatter in the atmosphere along the flight track in the North Atlantic. (*b*) Vertically resolved attenuation coefficients in the ocean along the flight segment between the dashed lines. From 35°N to ~40°N, the transect sampled oligotrophic conditions with significant subsurface features north of 38°N. A strong near-surface bloom was encountered between ~41°N and ~43°N, followed by more mesotrophic waters with significant subsurface features at depths between ~10 and 20 m. Abbreviations: HSRL-1, High-Spectral-Resolution Lidar 1; NAAMES, North Atlantic Aerosols and Marine Ecosystems Study; sr, steradian. Adapted from Hair et al. (2016).

NAAMES. These data, acquired from a flight altitude of 9 km, illustrate the calibration advantage of the HSRL technique. Similarly to a satellite viewing geometry, the optical paths traveled by the photons to and from the ocean include attenuating layers of smoke in the free troposphere and marine aerosol in the boundary layer, producing large variations in the strength of the ocean backscatter signals along the flight track. This would create a significant calibration challenge for the elastic backscatter technique but not for the HSRL (Hair et al. 2008, 2016).

The SABOR campaign provided an opportunity to compare HSRL-1 ocean retrieval products with independent measurements of the same properties. For example, **Figure 4*a*** shows an along-track comparison of HSRL-derived K_L at a depth of 10 m and MODIS K_D values collected on the same day, with excellent agreement between products. The HSRL-1 ocean products also show excellent agreement with optical properties measured at sea during SABOR. For example, **Figure 4*c*** and **Figure 4*d*** show comparisons of depth-resolved b_{bp} values from HSRL-1 with near-coincident in situ data from optical profiling casts at the SABOR ship stations (Schulien et al. 2017). These comparisons with MODIS and in situ data have correlation coefficients of $\geq$0.94 and slopes of $\sim$1.0, demonstrating the accuracy of HSRL ocean retrievals.

Schulien et al. (2017) used in situ and HSRL-1 data from SABOR to quantify the value of vertically resolved measurements of b_{bp} and K_D for improving estimates of net primary production relative to estimates based solely on the surface properties retrievable from passive ocean color data. Analysis of SABOR data indicated that surface-weighted ocean-color-like properties yielded estimates of water column–integrated net primary production that consistently underestimated values calculated with vertically resolved data, with errors of up to 54% (Schulien et al. 2017). The vertical plankton structure during SABOR was modest at best, and previous estimates of net primary production errors associated with a wider range in vertical structure indicate that such errors can exceed 100% (Platt & Sathyendranath 1988, Hill & Zimmerman 2010, Churnside 2015). These findings demonstrate the importance of plankton vertical structure for accurate assessments of ocean plankton stocks, productivity, and carbon cycling.

In addition to retrieving ocean optical and plankton properties, lidar measurements might also provide insight into physical mixing processes (Zawada et al. 2005). Specifically, the expectation is that particle concentrations in the active turbulent mixing layer will be homogeneous with depth. Accordingly, detection of subsurface scattering layers can be used to delineate the maximum depth of active mixing. This constraint on active mixing can be used as a global data set for testing physical mixing models and has the potential to significantly improve understanding of dynamic relationships among physics, plankton biomass, and bloom trajectories.

5. THE DAWN OF SATELLITE LIDAR IN OCEANOGRAPHY

CZCS was certainly not the best satellite sensor ever built to globally sample surface ocean properties, but it was the first. The idea of deriving plankton properties from remotely detectable optical signals significantly predates CZCS, and the concept had been demonstrated from aircraft (Clarke et al. 1970). But eventually the time comes to bite the bullet and launch a proof-of-concept instrument into space. The launch of CZCS was that proof of concept for ocean color and a landmark event. The dawn of the satellite lidar era in oceanography shares some parallels with this CZCS story in that the lidar approach was initially demonstrated with airborne sensors (to a far greater degree than CZCS, in fact), and the first satellite demonstration was based on an instrument with limited capabilities. Unlike the CZCS story, however, the satellite lidar instrument was designed with no intention of retrieving properties of the ocean. That lidar was CALIOP.

As discussed above, CALIOP is a simple elastic backscatter lidar with emissions at 532 and 1,064 nm, but in-water attenuation of the latter band is too great to provide any useful information about

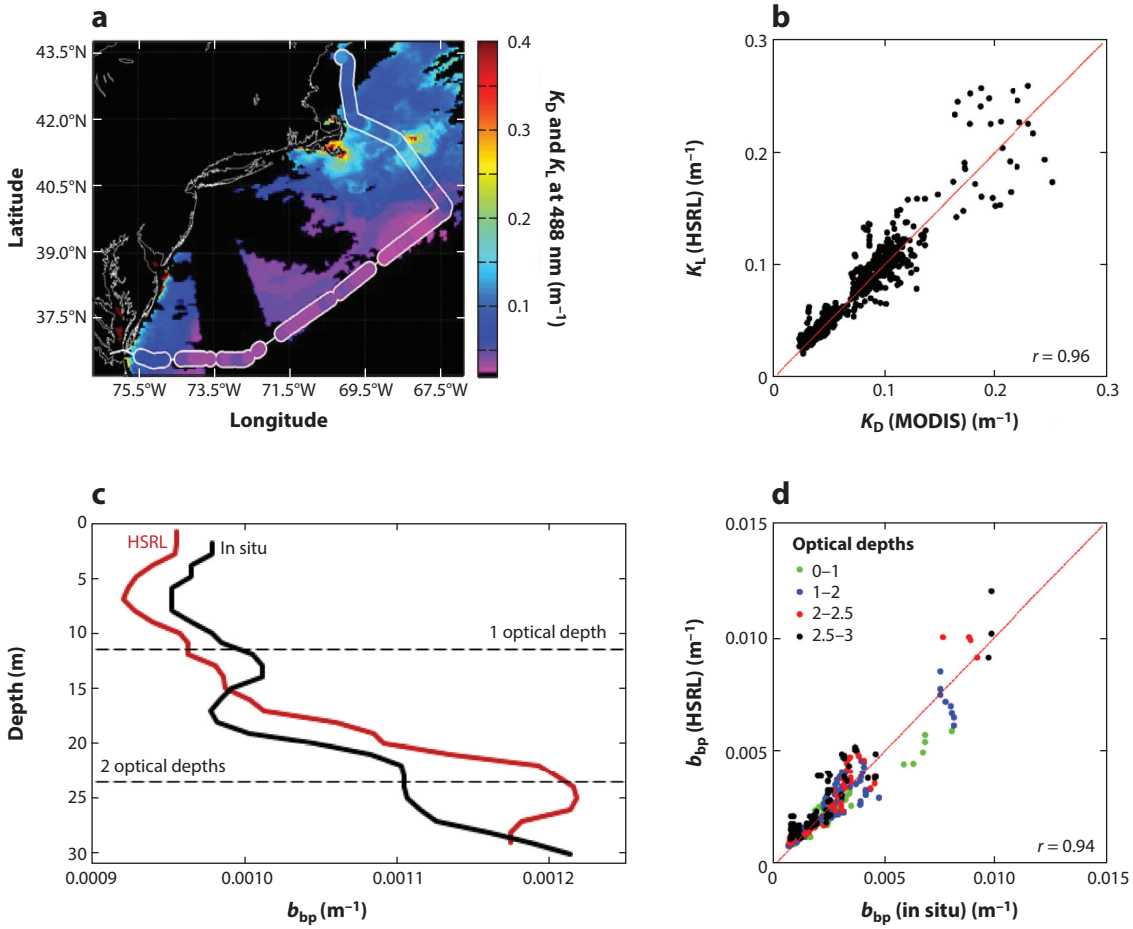

Figure 4

Results from the SABOR field campaign, which encompassed 24 flights with the HSRL-1 and 23 ocean sampling stations on the R/V *Endeavor*. (*a*) MODIS K_D values at 488 nm (Lee et al. 2005) for July 18, 2014 (*background color*), and K_L retrieved with HSRL-1 along a flight track on the same day (*white outlined data*). HSRL-1 K_L values were calculated at a depth of 10 m and converted to 488 nm by accounting for the difference in pure seawater absorption. (*b*) K_L–K_D matchup data from HSRL-1 and MODIS for all flights during the SABOR campaign. (*c*) Comparison of b_{bp} profiles from HSRL-1 (532 nm, *red line*) and in situ measurements (529 nm, *black line*) from a WET Labs ECO BB3 instrument. (*d*) Matchup comparison of HSRL-1 and in situ b_{bp} data from the 16 offshore SABOR stations where overboard optical casts had near-coincident HSRL measurements. Colors indicate the optical depth of each sample. Abbreviations: ECO, Environmental Characterization Optics; HSRL-1, High-Spectral-Resolution Lidar 1; MODIS, Moderate Resolution Imaging Spectroradiometer; SABOR, Ship-Aircraft Bio-Optical Research. Panels *a* and *b* adapted from Hair et al. (2016); panels *c* and *d* adapted from Schulien et al. (2017).

subsurface ocean properties. CALIOP's 23-m vertical resolution was designed for atmospheric science applications and is too coarse for ocean profiling applications. In addition, backscatter from the ocean surface creates an artifact in CALIOP's co-polarized subsurface data. CALIOP also lacks the advanced capabilities of an HSRL system, so it does not provide the direct information required for independently separating the attenuation and backscattering components from the retrieved subsurface signal. However, what CALIOP does provide is a space-based measurement of an ocean signal at 532 nm from its cross-polarization channel. In addition, this ocean signal

is measured at a constant viewing angle, is independent of solar angle, and is retrieved both day and night and through significant cloud and aerosol layers. The CALIOP orbit also has a 16-day repeat cycle that provides a globally representative sampling of ocean ecosystems (**Figure 5*a***). Thus, although CALIOP was not the optimal lidar system for observing the ocean, it has yielded not only the first space-based proof of concept, but significant scientific results as well.

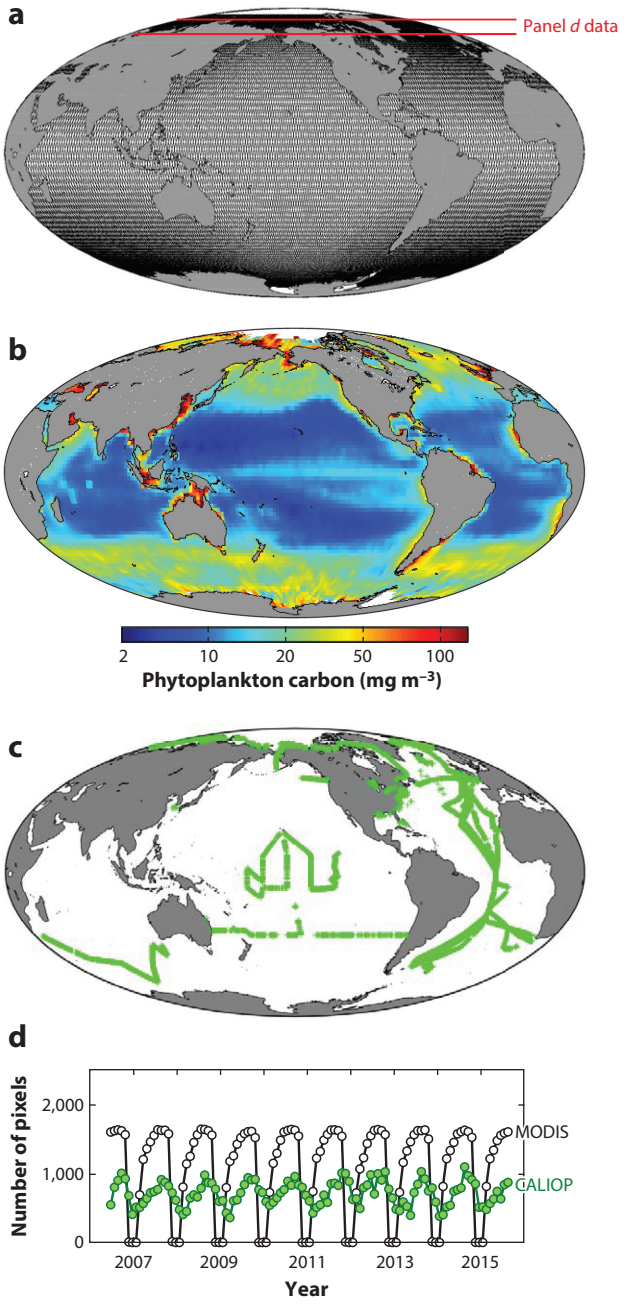

The first challenge in using CALIOP data for oceanographic research was isolating the subsurface signal in a calibrated and quantitative manner. This was accomplished by employing the ratio of cross-polarized to co-polarized signal returns (the depolarization ratio), which is well calibrated through the atmosphere and ocean column because both channels respond similarly to absorption and scattering losses. The algorithm employed the sum of the depolarization ratio from the first few bins below the ocean surface, an estimate of the backscatter from the ocean surface itself, K_D values from MODIS, and assumptions based on empirical data to generate a surface-weighted column estimate of b_{bp} (for details, see the supplementary materials for Behrenfeld et al. 2013).

The second challenge in using CALIOP data was to validate the ocean products. An ideal opportunity for this arose from a NASA-funded airborne field campaign based in the Azores that was coupled to ship-based optical measurements conducted as part of a UK Atlantic Meridional Transect cruise (Behrenfeld et al. 2013). The validation component of the lidar study focused on ship, aircraft, MODIS, and CALIOP measurements of b_{bp}. For the overall ship transect data, the study found a significantly better agreement between in situ b_{bp} and CALIOP retrievals ($r^2 = 0.54$) than for the MODIS ocean color retrievals ($r^2 = 0.13$ and 0.27 for different inversion algorithms). For the three aircraft flights of the campaign, CALIOP retrievals were well aligned with airborne HSRL-1-based b_{bp} data ($r^2 = 0.58$). Overall, these results were viewed as highly encouraging, given that the ship, aircraft, and satellite data diverged significantly in spatial resolution and were not temporally coincident.

Given the success of the field validation analysis, Behrenfeld et al. (2013) then provided the first published global map of surface b_{bp} from a space-based lidar and associated estimates of phytoplankton carbon biomass (C_{phyto}) (**Figure 5*b***) and total particulate organic carbon (POC). These data were compared with MODIS-based b_{bp} values from the Garver-Siegel-Maritorena (GSM) inversion algorithm (Garver & Siegel 1997, Maritorena et al. 2002, Siegel et al. 2002) and the Quasi-Analytical Algorithm (QAA) (Lee et al. 2002) and associated C_{phyto} and POC values. The CALIOP-based products exhibited similar global distributions and seasonal cycles as the MODIS-based products but also highlighted some inconsistencies. For example, the CALIOP global POC data showed a dual-mode frequency distribution similar to that of the QAA but with peaks at lower POC concentrations, and a low-POC peak (~45 mg C m^3) that was consistent with (but of smaller magnitude than) the peak in GSM data (see figure S4 in Behrenfeld et al. 2013).

The Behrenfeld et al. (2013) study focused on the utility of satellite lidar measurements for global ocean studies, but lidar measurements may be especially important for specific regions and

Figure 5

Sampling of the global ocean with CALIOP. (*a*) CALIOP ground tracks achieved within a single 16-day repeat cycle. The red lines indicate the 55–65°N section used to compare CALIOP and MODIS data coverage in panel *d*. (*b*) CALIOP-based climatological annual average phytoplankton biomass (C_{phyto}) for the 2006–2012 period reported by Behrenfeld et al. (2013). (*c*) Location of all field b_{bp} data in the NASA SeaBASS data archive. These data required 13 years to collect yet still left most of the ocean unsampled in space and time. By comparison, a satellite lidar can provide globally representative sampling of b_{bp} every 16 days that can be used for ocean science investigations and to refine algorithms for passive ocean color retrievals. (*d*) Comparison of CALIOP and MODIS pixel coverage per month for the 55–65°N section identified in panel *a*. The filled and unfilled symbols indicate the total number of 1° latitude × 1° longitude ice-free ocean pixels per month with valid CALIOP and MODIS b_{bp} data, respectively. Abbreviations: CALIOP, Cloud-Aerosol Lidar with Orthogonal Polarization; MODIS, Moderate Resolution Imaging Spectroradiometer; SeaBASS, Sea-Viewing Wide Field-of-View Sensor (SeaWiFS) Bio-Optical Archive and Storage System. Panel *d* adapted from supplementary information in Behrenfeld et al. (2017).

scientific questions. One such example is an improved understanding of high-latitude ecosystems. As noted above, high-latitude regions present particularly challenging conditions for passive ocean color sensors. They tend to be plagued by persistent cloud cover, solar geometries change significantly during the year, and periods of polar night prevent any passive measurements at all over broad areas. Because of these challenges, incomplete ocean color records at high latitudes can completely miss critical events in plankton annual cycles. Here again, CALIOP has provided the first demonstration of how active lidar measurements from space can complement passive ocean color data to yield new scientific insights.

Convergence of CALIOP ground tracks yields the most dense spatial sampling at high latitudes (**Figure 5*a***), providing 1° binned spatial coverage comparable to that of MODIS in both the north and south polar regions during late-spring to early-autumn months and better coverage from the late-autumn to early-spring period (**Figure 5*d***). With these data, Behrenfeld et al. (2017) demonstrated that initiation of polar annual phytoplankton blooms generally occurs before conditions are suitable for passive ocean color retrievals. The CALIOP data further provided the clearest demonstration to date that annual cycles in polar phytoplankton biomass are driven, at the monthly timescale, by the rate of acceleration and deceleration in phytoplankton division rates. Accordingly, the climax of the bloom coincides with division rate maxima rather than with a decrease in division. The study also showed that interannual variability in the amplitude of the phytoplankton annual biomass cycle is related to the overall range in division rate between winter minima and summer maxima. Finally, the lidar data were used for a complete annual accounting of the relative contributions of ecological processes and ice cover changes to a decade of variations in polar phytoplankton biomass.

The lidar era in satellite oceanography has arrived.

6. A NEW LIGHT ON THE HORIZON

There are 1,107 words in the previous section; perhaps the three most important of these are "proof of concept." CALIOP provides a tantalizing glimpse of where lidar measurements can take us, but it is not a blueprint for future ocean satellite lidars. Transitioning a new measurement from ground-based observations to an on-orbit system has been the demise of many exciting new remote sensing concepts. The simple fact is that satellite missions are expensive, so launching a totally new technology is unnervingly risky compared with iteratively improving an existing approach. CALIOP has unintentionally provided this key step from a field-verified "good idea" to an on-orbit demonstrated capability. CALIOP is for satellite lidar what CZCS was for ocean color. It has shown us that an ocean signal is detectable from a space lidar. Now, it is time to think about what we can really achieve with a satellite lidar when it is actually built for ocean measurements.

There are three obvious targets for realizing major scientific advances from a space lidar, and each of these has airborne heritage: (*a*) improved vertical resolution of the detected signal, (*b*) an expanded set of detection bands, and (*c*) additional laser emission wavelengths. We discuss some of the science applications of these expanded capabilities in the following paragraphs.

Water column vertical structure is clearly resolved at 1–3-m resolution with airborne lidar sensors, and a similar scale can be envisioned for a future satellite lidar. With such capabilities, phytoplankton and total suspended particulate distributions within the upper light field could be characterized globally to enable improved estimates of net primary production and carbon stocks. A counterpart to improved vertical resolution is increased penetration of the retrieved signal. The maximum depth from which valid retrievals can be achieved with a satellite lidar is a function of multiple factors, including laser pulse energy and repetition rate, laser emission wavelength,

telescope size, horizontal averaging, and the optical clarity of the water column. As a rule of thumb, it is anticipated that an ocean-optimized satellite lidar can provide valid ocean properties to 3 optical depths. Such retrieval depths have already been demonstrated with airborne lidar. Thus, a space lidar can detect plankton properties within as much as 65% of the euphotic zone. Importantly, phytoplankton within this upper layer are the dominant contributors to water column–integrated primary production, and vertical distribution within this layer is a significant source of uncertainty in ocean color–based assessments of production (Platt & Sathyendranath 1988, Hill et al. 2013, Zhai et al. 2012, Schulien et al. 2017). In the permanently stratified ocean (roughly the ocean region between 40°N and 40°S), deep chlorophyll maxima are often found very near the bottom of the photic zone (i.e., >3.5 optical depths) (Cullen 1982, 2015) and thus are beyond the reach of a satellite lidar. In many cases, these deep chlorophyll maxima predominantly reflect light-driven changes in phytoplankton chlorophyll:carbon ratios (Fennel & Boss 2003) and can be effectively reconstructed with a photoacclimation model (e.g., Westberry et al. 2008). In other cases, deep chlorophyll maxima reflect changes in phytoplankton biomass, and characterizing these features will require augmenting satellite lidar measurements with additional technologies (see Section 8).

An ocean-optimized space lidar must also depart from the simple elastic backscatter approach employed by CALIOP and include additional measurement bands allowing direct separation of attenuation and backscattering coefficients through the water column. The HSRL technique (Section 4) represents one approach for achieving this requirement and has been extensively demonstrated in the field. The ability to directly separate attenuation and backscattering will greatly improve the accuracy of future ocean products and will make the lidar retrievals independent of ocean color data or bio-optical models. Accordingly, the lidar ocean products will provide an unprecedented global test data set (in terms of temporal and spatial coverage) for improving ocean color geophysical retrievals. Currently, development and validation of ocean color algorithms rely on field-collected data, which are sparse in time and terribly undersampled in space (**Figure 5*c***).

Another exciting avenue for advancement is expansion of the detection waveband set to include measurements of lidar-stimulated fluorescence. Airborne lidar systems have a long history of chlorophyll fluorescence measurements (Section 4). A similar space-based fluorescence measurement could serve multiple scientific applications. First, the total fluoresced light can be quantitatively related to pigment concentration. Because incident sunlight causes significant changes in the quantum yield of fluorescence (a process referred to as nonphotochemical quenching), lidar-based assessments of pigment concentration will be most accurate for measurements made on the dark side of Earth. These chlorophyll assessments, in turn, can be used to distinguish phytoplankton pigment contributions to measured K_D from that of other absorbing compounds. An important benefit of the lidar fluorescence measurements compared with passive fluorescence measurements is that, obviously, the passive measurements cannot be collected at night and thus suffer from uncertainties in nonphotochemical quenching.

The benefit of a lidar chlorophyll fluorescence channel goes beyond simply providing an estimate of pigment concentration. An ability to measure unquenched fluorescence at night could improve descriptions of daytime nonphotochemical quenching variability and thus allow more accurate interpretations of ocean color–based fluorescence data. Lidar-based nonphotochemical quenching assessments could further be evaluated in terms of different types of phytoplankton assemblages, thus providing new insight on photoacclimation strategies. A final benefit from a lidar fluorescence channel is that it may provide information on iron-limited growth conditions, an application that will require coincident ocean color data. Iron stress in the presence of high

macronutrients results in the synthesis of nonfunctional pigment-protein complexes that affect fluorescence quantum yields (Behrenfeld et al. 2006, Schrader et al. 2011, Behrenfeld & Milligan 2013). Quantum yields could be assessed by normalizing lidar-measured fluorescence signals to ocean color–based pigment absorption at 532 nm (a product from a spectral inversion algorithm), potentially allowing detection of these unique complexes and thus mapping of iron-stressed populations.

A final avenue for advancing ocean satellite lidar capabilities is increasing laser spectral emissions to a three-wavelength system of 355, 532, and 1,064 nm. The addition of a 355-nm source could provide multiple benefits. First, under oceanographic conditions of low CDOM, 355 nm can penetrate deeper into the water column than 532 nm. Perhaps more importantly, the combination of 355 and 532 nm can provide critical information on water column constituents. On the absorption side, CDOM exhibits an exponential increase in absorption with decreasing wavelength, whereas phytoplankton pigment absorption peaks in the visible wavelengths and tends to decrease in the near-ultraviolet wavelengths. Thus, the 355-nm lidar measurement would enable some separation skill between absorption by CDOM and absorption by pigments. Differences in backscatter coefficients at 355 and 532 nm could similarly provide information on the slope of the particle size distribution, enabling improved assessments of phytoplankton biomass and total particulate carbon stocks. Here again it is important to emphasize the value of the HSRL technique, as the accuracy of these important advanced geophysical retrievals will be significantly compromised for a simple elastic scattering lidar.

In closing this section, we note that cloud and aerosol measurements from the ocean-optimized lidar described above would have powerful crosscutting applications in science at the ocean-atmosphere interface and atmospheric science in general. As highlighted in the Intergovernmental Report on Climate Change report (IPCC 2013), clouds and aerosols are the largest drivers of uncertainty in estimates of Earth's energy budget. Accurate measurements of aerosol extinction at 532 nm from a spaceborne HSRL would provide significantly improved estimates of aerosol direct radiative effects compared with CALIOP (Thorsen et al. 2017). The 532-nm extinction measurements would also provide a much improved satellite-based proxy for the concentration of cloud condensation nuclei than is possible from passive sensors (Stier 2016), benefiting studies of aerosol-cloud interactions. A polarization-sensitive lidar with elastic backscatter channels at 1,064 nm and HSRL channels at 532 nm would provide curtains of aerosol type [i.e., marine aerosol, continental pollution, biomass smoke, or dust (Burton et al. 2012, 2014)], which would be useful for assessing and improving chemical transport models. The addition of HSRL channels at 355 nm would enable vertically resolved retrievals of aerosol effective radius and concentration (Müller et al. 2014, Sawamura et al. 2017), further improving retrievals of cloud condensation nuclei and providing useful data for air quality applications. High vertical resolution and HSRL capability will also significantly improve retrievals of cloud microphysical properties (phase, droplet concentration, and liquid water content), building on the work of Hu (2007) and Hu et al. (2007).

As a primer for thought and discussion regarding a future mission, **Table 1** provides a "shopping list" summary of the enhanced capabilities described in this section and a list of added scientific value associated with each.

7. AN OPTIMIZED OCEAN-ATMOSPHERE SATELLITE LIDAR

In this section, we put on our engineering hats to consider design elements of an ocean-atmosphere optimized lidar with the capabilities discussed in Section 6, with our particular example (**Figure 6**) based on the HSRL technique. In this design, the pulsed laser transmitter is seeded by a low-power

Table 1 Summary of the increase in science value with capability starting from a CALIOP-like base case

	Sensor capability	Added value to ocean science	Added value to atmospheric science
CALIOP equivalent	Elastic backscatter technique at 532 and 1,064 nm Depolarization at 532 nm Vertical resolution of 23 m for the ocean and 30 m for the atmosphere	Surface-weighted b_{bp} and K_D (not independent) Sampling through aerosol layers and tenuous clouds Sampling regardless of sun angle Day-night comparisons possible	Aerosol and cloud vertical distributions and properties (optical, microphysical, and bulk) derived from attenuated backscatter and depolarization profiles
Above plus	Vertical resolution of <3 m	Crude estimates of profile-average K_D; unknown error resulting from vertical variability in K_D and b_{bp} Crude b_{bp} profiling capability (calibration will be an issue)	Improved estimates of cloud microphysical properties (phase, droplet concentration, and liquid water content)[a]
Above plus	HSRL at 532 nm Depolarization at 1,064 nm	Accurate independent profiles of b_{bp} and K_D at 532 nm Calibration accurate through ocean column Estimates of C_{phyto}, POC, and chlorophyll concentration Vertically resolved estimates of net primary production	Accurate independent profiles of aerosol extinction and backscatter Improved aerosol typing Estimates of cloud condensation nuclei concentration Advanced estimates of cloud microphysical properties
Above plus	Chlorophyll fluorescence	Improved estimates of chlorophyll concentration Nonphotochemical quenching Iron stress	
Above plus	HSRL at 355 nm Depolarization at 355 nm	Accurate independent profiles of b_{bp} and K_D at 532 and 355 nm Independent estimates of CDOM and pigment absorption Information on the slope of the particle size distribution Increased accuracy in vertically resolved net primary production	Aerosol effective radius and concentration Particulate air quality estimates Advanced cloud condensation nuclei estimates

The first row of the table represents a CALIOP-like base case, which is then followed by additional rows associated with an added capability and the value added for ocean and atmospheric sciences. Abbreviations: CALIOP, Cloud-Aerosol Lidar with Orthogonal Polarization; CDOM, colored dissolved organic matter; HSRL, high-spectral-resolution lidar; POC, particulate organic carbon.

[a]Retrievals of droplet concentration and liquid water content require additional coincident passive radiometric measurements.

continuous-wave 1,064-nm laser to ensure narrowband frequency-stable output. The fundamental 1,064-nm output of the pulsed laser is frequency doubled to 532 nm and tripled to 355 nm, providing output pulses at all three wavelengths. The receiver begins with a telescope of 1–1.5-m diameter, similar to CALIOP. Light collected by the telescope is focused into a field stop that defines the receiver field of view, which closely matches the divergence of the transmitted beam to minimize collection of diffusely scattered sunlight while still collecting most of the backscattered laser light. The light is then re-collimated into a small-diameter beam (e.g., 2–3 cm) in the receiver. Dichroic beam splitters separate the various wavelengths for additional optical processing. Narrowband solar rejection filters reduce the magnitude of scattered sunlight remaining within

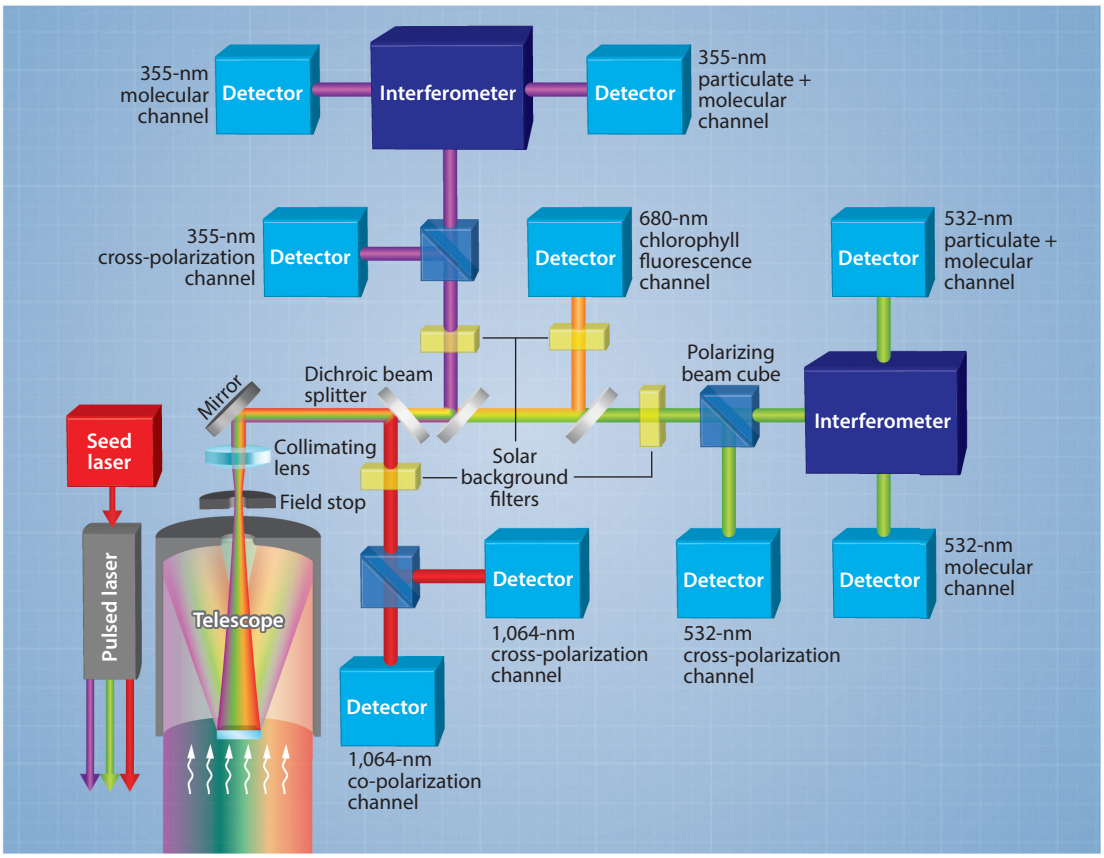

Figure 6

Simplified block diagram of the primary components in an advanced spaceborne ocean-atmosphere-optimized lidar.

the field of view. Polarizing beam cubes resolve the backscatter into polarization components that are parallel and perpendicular to the linear polarization of the transmitted laser pulses.

The HSRL technique is implemented in the design (**Figure 6**) using interferometric optical filters separating the received backscatter onto two detectors: one that measures backscatter predominantly from water or air molecules (the molecular channel) and one that measures a combination of particulate and molecular backscatter (the particulate channel). As discussed in Section 4, the two HSRL channels essentially provide two equations to solve for two unknowns: K_D and β_P. Finally, the design includes a channel for measuring the chlorophyll fluorescence signal in the 680-nm region.

The detection electronics would sample the measured signals at a vertical resolution of 1 m, and the laser temporal pulse width would correspond to a vertical resolution of 1–2 m, depending on the design of the laser. The fundamental along-track horizontal resolution is determined by the receiver field of view and laser repetition rate. A field of view set to achieve a 90-m footprint diameter at Earth's surface would be consistent with CALIOP. Setting the laser repetition rate to >80 pulses per second achieves a footprint separation of <90 m, ensuring contiguous along-track

sampling. With only a 90-m swath, orbital geometry must be considered to appreciate horizontal sampling. Our envisioned lidar mission would have a sun-synchronous orbit similar to that of CALIOP, which provides ~15 Earth orbits per day, repeats these orbits every 16 days, and yields the global sampling grid shown in **Figure 5*a***.

The ocean-atmosphere-optimized lidar design described here would enable unprecedented scientific advances. To date, the European Space Agency has built a 355-nm HSRL scheduled to launch on the Earth Cloud Aerosol and Radiation Explorer (EarthCARE) satellite in 2019. NASA has also invested significantly in the maturation of lidar technology, achieving all of the capabilities mentioned above and in Section 6. In fact, one lidar design for the Aerosols-Clouds-Ecosystems (ACE) mission concept incorporates all of the capabilities discussed above except for the chlorophyll fluorescence channel. Other NASA programs have contributed to the maturation of that design, and an airborne prototype with the capabilities recommended herein is due for flight demonstration in 2018. The bottom line is that a satellite ocean-atmosphere-optimized lidar can be realized in the near future.

8. VISION OF A VIRTUAL CONSTELLATION

Oceanographic research with satellite lidars is in its infancy. We hope that this review has provided a useful description of the lidar technique, an interesting narrative of its history in marine applications, an exciting account of recent achievements with the satellite CALIOP sensor, and some forward-looking ideas on future scientific pursuits with an advanced satellite lidar based on current technological capabilities.

Throughout this review, we have contrasted lidar measurements with traditional ocean color observations, but the most important message to take home from these comparisons is that each approach has its strengths and weaknesses. By focusing on the strengths of each technology, we can envision a synergistic future global ocean-observing constellation. At the core of this constellation is the pairing of an ocean-optimized HSRL-type satellite lidar and an advanced ocean color sensor (such as that planned for the PACE mission). This combination would maximize global spatial and temporal data coverage, introduce the vertical dimension into ecosystem characterizations, and allow cross-instrument data comparisons for algorithm development, improved ocean color atmospheric corrections, and an expansion in the diversity of retrieved geophysical properties.

Adding a multi-angle polarimeter to this constellation yields additional synergies. Polarimeters measure polarized radiances in multiple spectral bands and allow detailed characterization of aerosol optical depths and single-scatter albedo. These data would provide important constraints for ocean color atmospheric corrections and allow extrapolation of lidar atmospheric data between measurement curtains. Polarimetry can also distinguish mineral and biogenic particles in the upper water column (Loisel et al. 2008). Reciprocally, ocean color measurements provide constraints on water-leaving contributions to the signal measured by the polarimeter. The final piece of this integrated observing system is a global array of in situ Bio-Geo-Argo floats, providing sustained and coincident field validation data for the satellite sensors and a means for extending the satellite data to depths beyond the reach of a lidar.

Figure 7 is an artistic rendering of our envisioned ocean-observing system. Although an ocean-optimized lidar mission has yet to be commissioned, a two-instrument PACE mission could provide the advanced ocean color sensor and polarimeter, and components of a global Bio-Geo-Argo array are being deployed [e.g., the Southern Ocean Carbon and Climate Observations and Modeling (SOCCOM) program (**https://soccom.princeton.edu**)] or in development.

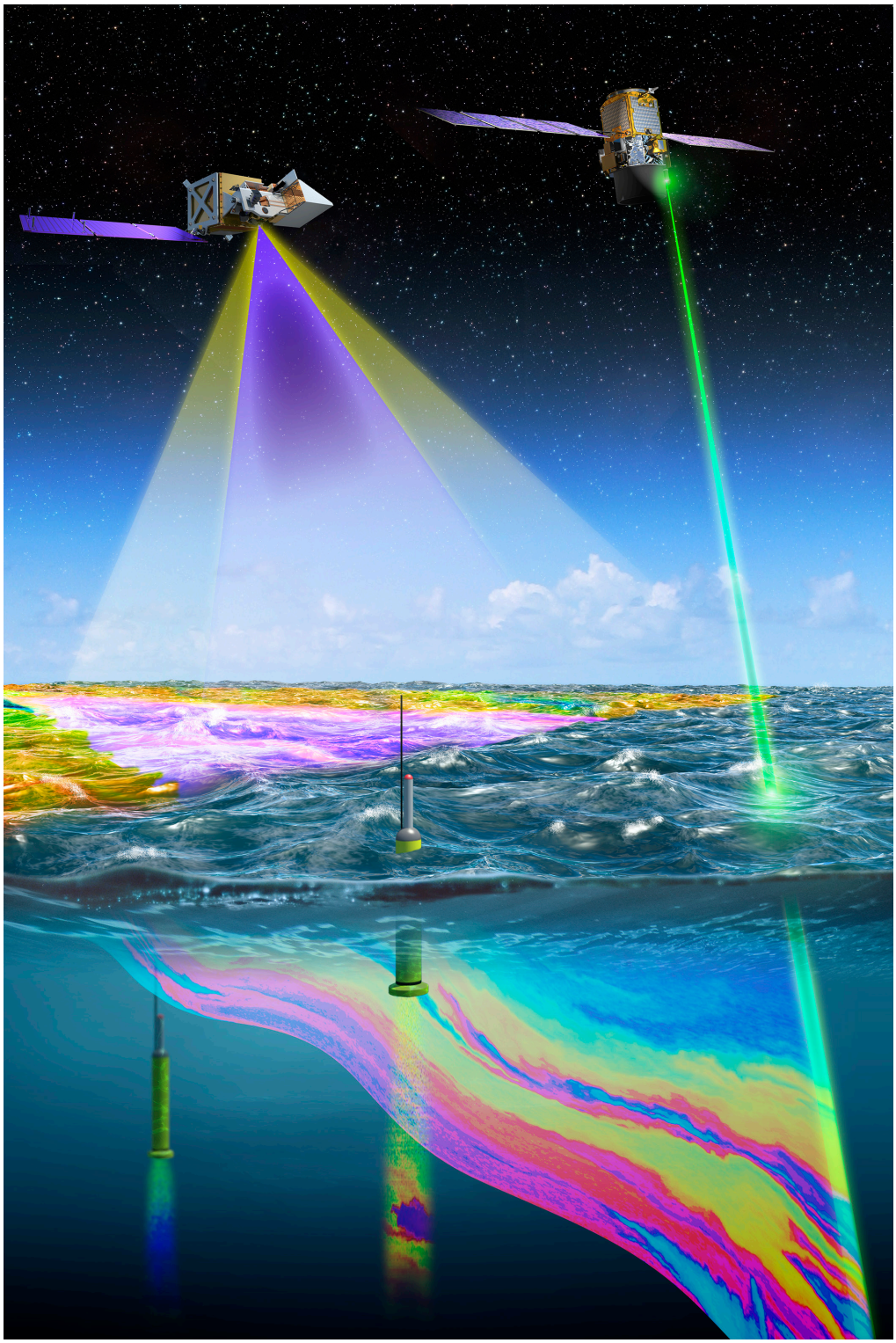

Figure 7

Artistic rendering of a future ocean-observing system encompassing in situ Bio-Geo-Argo floats and a satellite constellation that includes a high-spectral-resolution ocean-optimized lidar, an advanced ocean color sensor, and a multi-angle polarimeter.

DISCLOSURE STATEMENT

The authors are not aware of any affiliations, memberships, funding, or financial holdings that might be perceived as affecting the objectivity of this review.

ACKNOWLEDGMENTS

We thank the *Annual Review of Marine Science* for the invitation to provide this review, Dr. David Siegel for his insightful review of the manuscript, Dr. Emmanuel Boss for help on technical details, Mr. Timothy Marvel for help on illustrations, and NASA for funding on many grants and projects that have informed this review, including NAAMES, SABOR, and ACE.

LITERATURE CITED

Alvain S, Moulin C, Dandonneau Y, Breon F. 2005. Remote sensing of phytoplankton groups in case 1 waters for global SeaWiFS imagery. *Deep-Sea Res. I* 52:1989–2004

Antoine D, André J-M, Morel A. 1996. Oceanic primary production 2. Estimation at global scale from satellite (coastal zone color scanner) chlorophyll. *Glob. Biogeochem. Cycles* 10:57–69

Behrenfeld MJ, Boss E, Siegel DA, Shea DM. 2005. Carbon-based ocean productivity and phytoplankton physiology from space. *Glob. Biogeochem. Cycles* 19:GB1006

Behrenfeld MJ, Falkowski PG. 1997. Photosynthetic rates derived from satellite-based chlorophyll concentration. *Limnol. Oceanogr.* 42:1–20

Behrenfeld MJ, Hu Y, Hostetler CA, Dall'Olmo G, Rodier SD, et al. 2013. Space-based lidar measurements of global ocean carbon stocks. *Geophys. Res. Lett.* 40:4355–60

Behrenfeld MJ, Hu Y, O'Malley RT, Boss ES, Hostetler CA, et al. 2017. Annual boom-bust cycles of polar phytoplankton biomass revealed by space-based lidar. *Nat. Geosci.* 10:118–22

Behrenfeld MJ, Milligan AJ. 2013. Photophysiological expressions of iron stress in phytoplankton. *Annu. Rev. Mar. Sci.* 5:217–46

Behrenfeld MJ, Randerson JT, McClain CR, Feldman GC, Los SO, et al. 2001. Biospheric primary production during an ENSO transition. *Science* 291:2594–97

Behrenfeld MJ, Westberry TK, Boss E, O'Malley RT, Siegel DA, et al. 2009. Satellite-detected fluorescence reveals global physiology of ocean phytoplankton. *Biogeosciences* 6:779–94

Behrenfeld MJ, Worthington K, Sherrell RM, Chavez FP, Strutton P, et al. 2006. Controls on tropical Pacific Ocean productivity revealed through nutrient stress diagnostics. *Nature* 442:1025–28

Billard B, Abbot RH, Penny MF. 1986. Airborne estimation of sea turbidity parameters from the WRELADS laser airborne depth sounder. *Appl. Opt.* 25:2080–88

Boss E, Pegau WS. 2001. Relationship of light scattering at an angle in the backward direction to the backscattering coefficient. *Appl. Opt.* 40:5503–7

Bracher A, Vountas M, Dinter T, Burrows JP, Röettgers R, Peeken I. 2009. Quantitative observation of cyanobacteria and diatoms from space using PhytoDOAS on SCIAMACHY data. *Biogeosciences* 6:751–64

Bristow M, Nielsen D, Bundy D, Furtek R. 1981. Use of water Raman emission to correct airborne laser fluorosensor data for effects of water optical attenuation. *Appl. Opt.* 20:2889–906

Bruneau D, Pelon J, Blouzon F, Spatazza J, Genau P, et al. 2015. 355-nm high spectral resolution airborne lidar LNG: system description and first results. *Appl. Opt.* 54:8776–85

Bunkin AF, Surovegin AL. 1992. Lidar-aided measurement of phytoplankton chlorophyll and underwater scattering layers. *EARSeL Adv. Remote Sens.* 1:101–5

Burton SP, Ferrare RA, Hostetler CA, Hair JW, Rogers RR, et al. 2012. Aerosol classification using airborne high spectral resolution lidar measurements-methodology and examples. *Atmos. Meas. Tech.* 5:73–98

Burton SP, Vaughan MA, Ferrare RA, Hostetler CA. 2014. Separating mixtures of aerosol types in airborne high spectral resolution lidar data. *Atmos. Meas. Tech.* 7:419–36

Churnside JH. 2008. Polarization effects on oceanographic lidar. *Opt. Express* 16:1196–207

Churnside JH. 2014. Review of profiling oceanographic lidar. *Opt. Eng.* 53:051405

Churnside JH. 2015. Bio-optical model to describe remote sensing signals from a stratified ocean. *J. Appl. Remote Sens.* 9:095989

Churnside JH. 2016. Airborne lidar estimates of photosynthesis profiles. In *2016 IEEE International Geoscience and Remote Sensing Symposium (IGARSS)*, pp. 3777–80. New York: IEEE

Churnside JH, Demer DA, Mahmoudi B. 2003. A comparison of lidar and echosounder measurements of fish schools in the Gulf of Mexico. *ICES J. Mar. Sci.* 60:147–54

Churnside JH, Donaghay PL. 2009. Thin scattering layers observed by airborne lidar. *ICES J. Mar. Sci.* 66:778–89

Churnside JH, Marchbanks RD. 2015. Subsurface plankton layers in the Arctic Ocean. *Geophys. Res. Lett.* 42:4896–902

Churnside JH, Ostrovsky LA. 2005. Lidar observation of a strongly nonlinear internal wave train in the Gulf of Alaska. *Int. J. Remote Sens.* 26:167–77

Churnside JH, Sullivan JM, Twardowski MS. 2014. Lidar extinction-to-backscatter ratio of the ocean. *Opt. Express* 22:18698–706

Churnside JH, Wilson JJ, Tatarskii VV. 1997. Lidar profiles of fish schools. *Appl. Opt.* 36:6011–20

Churnside JH, Wilson JJ, Tatarskii VV. 2001. Airborne lidar for fisheries applications. *Opt. Eng.* 40:406–14

Clarke GL, Ewing GC, Lorenzen CJ. 1970. Spectra of backscattered light from the sea obtained from aircraft as a measure of chlorophyll concentration. *Science* 167:1119–21

Cullen JJ. 1982. The deep chlorophyll maximum: comparing vertical profiles of chlorophyll *a*. *Can. J. Fish. Aquat. Sci.* 39:791–803

Cullen JJ. 2015. Subsurface chlorophyll maximum layers: enduring enigma or mystery solved? *Annu. Rev. Mar. Sci.* 7:207–39

DeVries T, Primeau F, Deutsch C. 2012. The sequestration efficiency of the biological pump. *Geophys. Res. Lett.* 39:L13601

Esselborn M, Wirth M, Fix A, Tesche M, Ehret G. 2008. Airborne high spectral resolution lidar for measuring aerosol extinction and backscatter coefficients. *Appl. Opt.* 47:346–58

Falkowski PG, Barber RT, Smetacek V. 1998. Biogeochemical controls and feedbacks on ocean primary production. *Science* 281:200–6

Fennel K, Boss E. 2003. Subsurface maxima of phytoplankton and chlorophyll: steady state solutions from a simple model. *Limnol. Oceanogr.* 48:1521–34

Fernald FG. 1984. Analysis of atmospheric lidar observations—some comments. *Appl. Opt.* 23:652–53

Field CB, Behrenfeld MJ, Randerson JT, Falkowski PG. 1998. Primary production of the biosphere: integrating terrestrial and oceanic components. *Science* 281:237–40

Gantt B, Meskhidze N. 2013. The physical and chemical characteristics of marine primary organic aerosol: a review. *Atmos. Chem. Phys.* 13:3979–96

Garver SA, Siegel DA. 1997. Inherent optical property inversion of ocean color spectra and its biogeochemical interpretation: I. Time series from the Sargasso Sea. *J. Geophys. Res.* 102:18607–25

Gordon HR. 1982. Interpretation of airborne oceanic lidar: effects of multiple scattering. *Appl. Optics* 21:2996–3001

Hair JW, Hostetler CA, Cook AL, Harper DB, Ferrare RA, et al. 2008. Airborne high spectral resolution lidar for profiling aerosol optical properties. *Appl. Opt.* 47:6734–52

Hair JW, Hostetler CA, Hu Y, Behrenfeld MJ, Butler C, et al. 2016. Combined atmospheric and ocean profiling from an airborne high spectral resolution lidar. *EPJ Web Conf.* 119:22001

Hickman GD, Harding JM, Carnes M, Pressman A, Kattawar GW, Fry ES. 1991. Aircraft laser sensing of sound velocity in water: Brillouin scattering. *Remote Sens. Environ.* 36:165–78

Hill VJ, Matrai PA, Olson E, Suttles S, Steele M, et al. 2013. Synthesis of integrated primary production in the Arctic Ocean: II. In situ and remotely sensed estimates. *Prog. Oceanogr.* 110:107–25

Hill VJ, Zimmerman RC. 2010. Estimates of primary production by remote sensing in the Arctic Ocean: assessment of accuracy with passive and active sensors. *Deep-Sea Res. I* 57:1243–54

Hoge FE, Lyon PE, Swift RN, Yungel JK, Abbott MR, et al. 2003. Validation of Terra-MODIS phytoplankton chlorophyll fluorescence line height. I. Initial airborne lidar results. *Appl. Opt.* 42:2767–71

Hoge FE, Lyon PE, Wright CW, Swift RN, Yungel JK. 2005. Chlorophyll biomass in the global oceans: airborne lidar retrieval using fluorescence of both chlorophyll and chromophoric dissolved organic matter. *Appl. Opt.* 44:2857–62

Hoge FE, Swift RN. 1981. Airborne simultaneous spectroscopic detection of laser-induced water Raman backscatter and fluorescence from chlorophyll a and other naturally occurring pigments. *Appl. Opt.* 20:3197–205

Hoge FE, Swift RN, Yungel JK. 1995. Oceanic radiance model development and validation: application of airborne active-passive ocean color spectral measurements. *Appl. Opt.* 34:3468–76

Hoge FE, Wright CW, Krabill WB, Buntzen RR, Gilbert GD, et al. 1988. Airborne lidar detection of subsurface oceanic scattering layers. *Appl. Opt.* 27:3969–77

Hu Y. 2007. Depolarization ratio-effective lidar ratio relation: theoretical basis for space lidar cloud phase discrimination. *Geophys. Res. Lett.* 34:L11812

Hu Y. 2009. Ocean, land and meteorology studies using space-based lidar measurements. In *Recent Advances in Remote Sensing: Proceedings of the 5th WSEAS International Conference on Remote Sensing (REMOTE'09)*, ed. R Revetria, V Mladenov, N Mastorakis, pp. 47–50. Sofia, Bulg.: WSEAS. **https://ntrs.nasa.gov/search.jsp?R=20090037431**

Hu Y, Vaughan M, McClain C, Behrenfeld MJ, Maring H, et al. 2007. Global statistics of liquid water content and effective number concentration of water clouds over ocean derived from combined CALIPSO and MODIS measurements. *Atmos. Chem. Phys.* 7:3353–59

IPCC (Intergov. Panel Clim. Change). 2013. *Climate Change 2013: The Physical Science Basis. Contribution of Working Group I to the Fifth Assessment Report of the Intergovernmental Panel on Climate Change*. Ed. TF Stocker, D Qin, G-K Plattner, M Tignor, SK Allen, et al. Cambridge, UK: Cambridge Univ. Press

Jacox MG, Edwards CA, Kahru M, Rudnick DL, Kudela RM. 2015. The potential for improving remote primary productivity estimates through subsurface chlorophyll and irradiance measurement. *Deep-Sea Res. II* 112:107–16

Kim HH. 1973. New algae mapping technique by the use of an airborne laser fluorosensor. *Appl. Opt.* 12:1454–59

Kostadinov TS, Siegel DA, Maritorena S. 2010. Global variability of phytoplankton functional types from space: assessment via the particle size distribution. *Biogeosciences* 7:3239–57

Lee JH, Churnside JH, Marchbanks RD, Donaghay PL, Sullivan JM. 2013. Oceanographic lidar profiles compared with estimates from in situ optical measurements. *Appl. Opt.* 52:786–94

Lee ZP, Carder KL, Arnone RA. 2002. Deriving inherent optical properties from water color: a multi-band quasi-analytical algorithm for optically deep waters. *Appl. Opt.* 41:5755–72

Lee ZP, Darecki M, Carder KL, Davis CO, Stramski D, Rhea WJ. 2005. Diffuse attenuation coefficient of downwelling irradiance: an evaluation of remote sensing methods. *J. Geophys. Res.* 110:C02017

Lin H, Kuzminov FI, Park J, Lee S, Falkowski PG, Gorbunov MY. 2016. The fate of photons absorbed by phytoplankton in the global ocean. *Science* 351:264–67

Loisel H, Duforet L, Dessailly D, Chami M, Dubuisson P. 2008. Investigation of the variations in the water leaving polarized reflectance from the POLDER satellite data over two biogeochemical contrasted oceanic areas. *Opt. Express* 16:12905–18

Maritorena S, Siegel DA, Peterson AR. 2002. Optimization of a semianalytical ocean color model for global-scale applications. *Appl. Opt.* 41:2705–14

Martin JH, Coale KH, Johnson KS, Fitzwater SE, Gordon RM, et al. 1994. Testing the iron hypothesis in ecosystems of the equatorial Pacific Ocean. *Nature* 371:123–29

McClain CR. 2009. A decade of satellite ocean color observations. *Annu. Rev. Mar. Sci.* 1:19–42

McCoy DT, Burrows SM, Wood R, Grosvenor DP, Elliott SM, et al. 2015. Natural aerosols explain seasonal and spatial patterns of Southern Ocean cloud albedo. *Sci. Adv.* 1:e1500157

Meskhidze N, Nenes A. 2006. Phytoplankton and cloudiness in the Southern Ocean. *Science* 314:1419–23

Müller D, Hostetler CA, Ferrare RA, Burton SP, Chemyakin E, et al. 2014. Airborne Multiwavelength High Spectral Resolution Lidar (HSRL-2) observations during TCAP 2012: vertical profiles of optical and microphysical properties of a smoke/urban haze plume over the northeastern coast of the US. *Atmos. Meas. Tech.* 7:3487–96

NASA. 2012. *Pre-Aerosols, Clouds, and ocean Ecosystems (PACE) Mission Science Definition Team report*. Rep., NASA, Washington, DC. **https://pace.oceansciences.org/docs/pace_sdt_report_final.pdf**

O'Malley RT, Behrenfeld MJ, Westberry TK, Milligan AJ, Shang S, Yan J. 2014. Geostationary satellite observations of dynamic phytoplankton photophysiology. *Geophys. Res. Lett.* 41:5052–59

Platt T, Sathyendranath S. 1988. Oceanic primary production: estimation by remote sensing at local and regional scales. *Science* 241:1613–20

Poole LR, Esaias WE. 1982. Water Raman normalization of airborne laser fluorosensor measurements: a computer model study. *Appl. Opt.* 21:3756–61

Quinn PK, Bates TS. 2011. The case against climate regulation via oceanic phytoplankton sulphur emissions. *Nature* 480:51–56

Ryu JH, Han HJ, Cho S, Park YJ, Ahn YH. 2012. Overview of geostationary ocean color imager (GOCI) and GOCI data processing system (GDPS). *Ocean Sci. J.* 47:223–33

Sadeghi A, Dinter T, Vountas M, Taylor B, Altenburg-Soppa M, Bracher A. 2012. Remote sensing of coccolithophore blooms in selected oceanic regions using the PhytoDOAS method applied to hyper-spectral satellite data. *Biogeosciences* 9:2127–43

Sathyendranath S, Aiken J, Alvain S, Barlow R, Bouman H, et al. 2014. *Phytoplankton functional types from space*. Rep. 15, Int. Ocean-Colour Coord. Group, Dartmouth, Can.

Sathyendranath S, Platt T. 1989. Remote sensing of ocean chlorophyll: consequence of nonuniform pigment profile. *Appl. Opt.* 28:490–95

Sawamura P, Moore RH, Burton SP, Chemyakin E, Müller D, et al. 2017. HSRL-2 aerosol optical measurements and microphysical retrievals vs. airborne in situ measurements during DISCOVER-AQ 2013: an intercomparison study. *Atmos. Chem. Phys.* 17:7229–43

Schrader PS, Milligan AJ, Behrenfeld MJ. 2011. Surplus photosynthetic antennae complexes underlie diagnostics of iron limitation in a cyanobacterium. *PLOS ONE* 6:e18753

Schulien JA, Behrenfeld MJ, Hair JW, Hostetler CA, Twardowski MS. 2017. Vertically-resolved phytoplankton carbon and net primary production from a high spectral resolution lidar. *Opt. Express* 25:13577–87

Shipley ST, Tracy DH, Eloranta EW, Trauger JT, Sroga JT, et al. 1983. High spectral resolution lidar to measure optical scattering properties of atmospheric aerosols. 1: theory and instrumentation. *Appl. Opt.* 22:3716–24

Siegel DA, Maritorena S, Nelson NB, Behrenfeld MJ. 2005. Independence and interdependencies of global ocean color properties: reassessing the bio-optical assumption. *J. Geophys. Res.* 110:C07011

Siegel DA, Maritorena S, Nelson NB, Hansell DA, Lorenzi-Kayser M. 2002. Global distribution and dynamics of colored dissolved and detrital organic materials. *J. Geophys. Res.* 107:3228

Silsbe GM, Behrenfeld MJ, Halsey KH, Milligan AJ, Westberry TK. 2016. The CAFE model: a net production model for global ocean phytoplankton. *Glob. Biogeochem. Cycles* 30:1756–77

Steinvall KO, Koppari KR, Karlsson UC. 1993. Experimental evaluation of an airborne depth-sounding lidar. *Opt. Eng.* 32:1307–21

Stier P. 2016. Limitations of passive remote sensing to constrain global cloud condensation nuclei. *Atmos. Chem. Phys.* 16:6595–607

Stramska M, Stramski D. 2005. Effects of a nonuniform vertical profile of chlorophyll concentration on remote-sensing reflectance of the ocean. *Appl. Opt.* 44:1735–47

Thorsen TJ, Ferrare RA, Hostetler CA, Vaughan MA, Fu Q. 2017. The impact of lidar detection sensitivity on assessing aerosol direct radiative effects. *Geophys. Res. Lett.* 44:9059–67

Werdell PJ, Franz BA, Bailey SW, Feldman GC, Boss E, et al. 2013. Generalized ocean color inversion model for retrieving marine inherent optical properties. *Appl. Opt.* 52:2019–37

Westberry TK, Behrenfeld MJ, Milligan AJ, Doney SC. 2013. Retrospective satellite ocean color analysis of purposeful and natural ocean iron fertilization. *Deep-Sea Res. I* 73:1–16

Westberry TK, Behrenfeld MJ, Siegel DA, Boss E. 2008. Carbon-based primary productivity modeling with vertically resolved photoacclimation. *Glob. Biogeochem. Cycles* 22:GB2024

Winker DM, Vaughan MA, Omar A, Hu Y, Powell KA, et al. 2009. Overview of the CALIPSO mission and CALIOP data processing algorithms. *J. Atmos. Ocean. Technol.* 26:2310–23

Yoder JA, Aiken J, Swift RN, Hoge FE, Stegmann PM. 1993. Spatial variability in near-surface chlorophyll a fluorescence measured by the Airborne Oceanographic Lidar (AOL). *Deep-Sea Res. II* 40:37–53

Zawada DG, Zaneveld J, Ronald V, Boss E, Gardner WD, et al. 2005. A comparison of hydrographically and optically derived mixed layer depths. *J. Geophys. Res.* 110:C11001

Zhai L, Gudmundsson K, Miller P, Peng W, Guðfinnsson H, et al. 2012. Phytoplankton phenology and production around Iceland and Faroes. *Cont. Shelf Res.* 37:15–25